Inverse Problems

PAPER

# A non-iterative approach to inverse elastic scattering by unbounded rigid rough surfaces



IOP Publishing Inverse Problems

Inverse Problems **35** (2019) 025007 (20pp) https://doi.org/10.1088/1361-6420/aaf3d6

# A non-iterative approach to inverse elastic scattering by unbounded rigid rough surfaces

**Guanghui Hu**[1], **Xiaoli Liu**[2,3], **Bo Zhang**[3,4] and **Haiwen Zhang**[5]

[1] Beijing Computational Science Research Center, Beijing 100193, People's Republic of China
[2] Academy of Mathematics and Systems Science, Chinese Academy of Sciences, Beijing 100190, People's Republic of China
[3] School of Mathematical Sciences, University of Chinese Academy of Sciences, Beijing 100049, People's Republic of China
[4] LSEC, NCMIS and Academy of Mathematics and Systems Science, Chinese Academy of Sciences, Beijing, 100190, People's Republic of China
[5] NCMIS and Academy of Mathematics and Systems Science, Chinese Academy of Sciences, Beijing 100190, People's Republic of China

E-mail: hu@csrc.ac.cn, liuxiaoli@amss.ac.cn, b.zhang@amt.ac.cn and zhanghaiwen@amss.ac.cn

Received 6 April 2018, revised 6 November 2018
Accepted for publication 26 November 2018
Published 2 January 2019

**Abstract**

This paper is concerned with the inverse time-harmonic elastic scattering problem of recovering unbounded rough surfaces in two dimensions. We assume that elastic plane waves with different directions are incident onto a rigid rough surface in a half plane. The elastic scattered field is measured within a finite distance above the rough surface. A sampling-type imaging algorithm is proposed to recover the unbounded rough surface from the scattered near-field data, which involves only inner products between the data. Numerical experiments are presented to show that the inversion scheme is not only efficient but also accurate and robust with respect to noise.

Keywords: inverse elastic scattering, unbounded rough surface, Navier equation, Dirichlet boundary condition, near-field data

(Some figures may appear in colour only in the online journal)

## 1. Introduction

In this paper, we study the inverse scattering problem of time-harmonic elastic waves by an unbounded rough surface in two dimensions. The region above the surface is filled with a homogeneous and isotropic elastic medium, while the material below is assumed to be elastically rigid. Our goal is to recover the unbounded interface from the scattered field measured at a finite distance above the rough surface. Such kind of inverse problems occurs in many applications such as geophysics, seismology and nondestructive testing [8, 24, 32]. Though a traction-free boundary condition or a transmission interface condition may have more applications in practice, we only consider scattering surfaces of Dirichlet kind, which means that the medium beneath the rough surface is rigid in elasticity. We note that the well-posedness of forward elastic scattering problems is well-understood in a two dimensional setting by applying either the integral equation method [4–6] or variational approach [16, 18]. See figure 1 for an illustration of the scattering problem in a globally perturbed half plane.

Given an incident field and the rough surface, the forward problem is to determine the field distribution of the scattered field. Uniqueness and existence of forward solutions have been investigated in [4–6] by the integral equation method and in [16, 18] by the variational method. These approaches extend the solvability results for grating diffraction problems to the more challenging case of unbounded rough surfaces in elasticity. In the periodic case, numerical methods such as the two-step optimization method [17], the factorization method [21] and the transformation-based near-field imaging method [27, 28] have been proposed to solve the inverse elastic scattering problems for diffraction gratings. Note that the periodic setting significantly simplifies the arguments for the case of general rough surfaces. However, relatively little studies are carried out for inverse elastic scattering arising from global rough surfaces and it is not trivial to extend the above mentioned methods to inverse rough surface scattering problems. We refer to [15] for a recent application of the linear sampling method (see [14] for bounded scatterers) to recover locally perturbed sound-soft rough surfaces, which however does not work for general rough surfaces. This is mainly due to infiniteness and irregularity of globally rough surfaces, which bring additional difficulties not only to mathematical analysis but also to numerical computation. In practice, the measurement positions are always restricted to a finite sub-domain. Hence, it is in general impossible to recover the entire rough surface from these limited data. Intuitively, only the scattering surface closest to the measurement positions can be best reconstructed, although the other part may also affect the data. In our numerical experiments, by using the limited measurement data, we can only reconstruct part of the rough surface. However, our theoretical analysis in section 3 shows that the whole rough surface can be retrieved if the near field data over an infinite line above the surface are available.

In this paper, we shall propose a non-iterative imaging approach to reconstruct the unbounded rough surface below the measurement positions from the near-field data generated by elastic plane waves at one frequency with multiple directions. The proposed approach is of sampling type which does not require forward solvers in the inversion process. We take inspirations from recent studies for inverse acoustic scattering problems, for example, the orthogonality sampling method [31], topological derivative-based approach [7, 9, 19], the direct sampling method [22, 29] and the reverse time migration method [11]. Note also that direct imaging methods have also been developed in [12, 23] for inverse elastic scattering by bounded obstacles. Compared to iterative schemes and other sampling type methods, the features of our imaging method include: (i) capability of depicting the profile of the surface only through computing the inner products of the measured data and a known function at each sampling point. Thus, the computational cost is very cheap. This merit is especially important

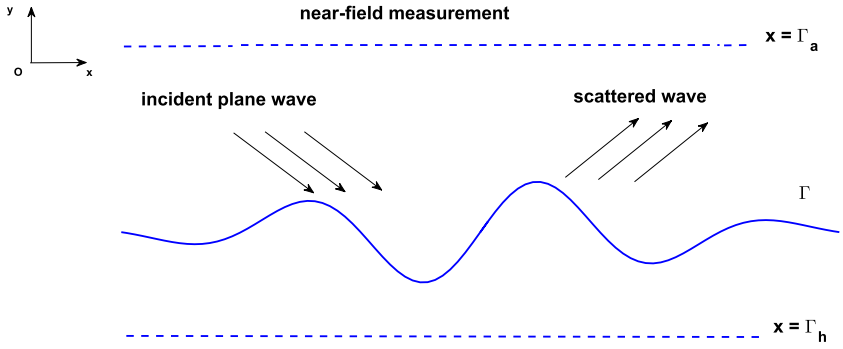


**Figure 1.** Inverse elastic scattering from an unbounded rough surface $\Gamma$. The measurement line segment $\Gamma_a$ means the positions for taking the near-field data above the scattering surface. Assuming that elastic plane waves are incident from above, we investigate the inverse scattering problem of determining $\Gamma$ in two dimensions. For simplicity, it is supposed throughout this paper that the Dirichlet boundary condition condition is imposed on $\Gamma$.

for elastic scattering problems since the computation for vectorial equations is usually more time-consuming than for scalar equations. In $N \geqslant 2$ dimensions, the computational cost for solving the Navier equation is at least $N$-times larger than the Helmholtz equation, and the cost for the inner product required by our scheme is $2^N$-times larger than the scalar case. (ii) Robustness to a fairly large amount of noise in the measured data. This paper focuses on the unbounded rough surface identification problem in linear elasticity and is an extension of our recent work [30] on near-field imaging penetrable interfaces modelled by the Helmholtz equation to the *Navier* equation. The elasticity problem takes a more complicated form than the acoustic case, due to the coexistence of the compressional and shear waves that propagate at different speeds. We consider only impenetrable rigid rough surfaces (on which the elastic displacement vanishes), but our method applies naturally to interfaces with other boundary or transmission conditions.

Our imaging scheme relies essentially on a relation between the Funk–Hecke formula and the free-space Green's tensor for the *Navier* equation; see (3.4) or (3.9). Motivated by this relation, we present the scattered field in the form of a superposition of incident elastic plane waves (see theorem 3.3 below). This expression of the scattered field will be proven to have the same decaying property as the imaginary part of the Green's tensor, as the sampling point moves away from the scattering surface. This yields our indicator function using elastic plane waves with different directions in a half plane. Numerical experiments are presented to show the effectiveness of our method. Further, we investigate the effect of the reconstructed results from the parameters such as the incident frequency, the measurement place and the noise level. Numerics show that our imaging algorithm is fast, accurate and very robust with respect to the noisy data.

The remainder of this paper is organized as follows. In section 2, we briefly review the well-posedness of the forward scattering problem using the integral equation method. Section 3 is devoted to an analysis of our imaging function and a description of the imaging algorithm. Numerical experiments are carried out in section 4 to demonstrate the effectiveness of the proposed approach.

## 2. Forward scattering problem

In the section we review existence and uniqueness of solutions to elastic scattering from rigid rough surfaces in two dimensions. The solvability of the second kind integral operator established in [6] will be used to analyze our indicator function to be proposed in section 3.

Consider a one-dimensional unbounded rough surface $\Gamma = \{x \in \mathbb{R}^2 \mid x_2 = f(x_1), x_1 \in \mathbb{R}\}$, where $\Gamma$ is supposed to be smooth enough such that $f \in BC^{1,1}(\mathbb{R})$. Here, $BC^{1,1}(\mathbb{R}) := \{\varphi \in BC(\mathbb{R}) \mid \varphi' \in BC(\mathbb{R}), j = 1, 2\}$ under the norm $\|\varphi\|_{1,\mathbb{R}} := \|\varphi\|_{\infty,\mathbb{R}} + \|\varphi'\|_{\infty,\mathbb{R}}$ and $BC(\mathbb{R})$ is the set of bounded and continuous functions in $\mathbb{R}$. Denote the region above $\Gamma$ by $\Omega$. Assume that $\Omega$ is filled with an isotropic homogeneous elastic medium characterized by the Lamé constants $\mu, \lambda$ with $\mu > 0, \lambda + \mu \geqslant 0$. For simplicity, we assume that the density function in $\Omega$ is normalized to be one and the region below $\Gamma$ is a rigid elastic body. Assume that a time-harmonic plane wave (with time variation of the form $\exp(-\mathrm{i}\omega t), \omega > 0$) is incident onto $\Gamma$ from $\Omega$. The incident plane wave $\boldsymbol{u}^{\mathrm{in}}$ can be either the compressional wave

$$\boldsymbol{u}_{\mathrm{p}}^{\mathrm{in}}(x; \boldsymbol{d}) := \boldsymbol{d}\mathrm{e}^{\mathrm{i}k_{\mathrm{p}}\boldsymbol{d}\cdot x},$$

or the shear wave

$$\boldsymbol{u}_{\mathrm{s}}^{\mathrm{in}}(x; \boldsymbol{d}) := \boldsymbol{d}^{\perp}\mathrm{e}^{\mathrm{i}k_{\mathrm{s}}\boldsymbol{d}\cdot x},$$

where $\boldsymbol{d} = (d_1, d_2)^T \in \mathbb{S} := \{x = (x_1, x_2) \mid |x| = 1\}$ is the incident direction and $\boldsymbol{d}^{\perp} = (-d_2, d_1)^T$. The compressional wave number $k_{\mathrm{p}}$ and the shear wave number $k_{\mathrm{s}}$ are given by

$$k_{\mathrm{p}} = \omega/\sqrt{\lambda + 2\mu}, \quad k_{\mathrm{s}} = \omega/\sqrt{\mu}.$$

The displacement of the total field $\boldsymbol{u} = (u_1, u_2)^T$ is then governed by the *Navier* equation

$$\mu\Delta\boldsymbol{u} + (\lambda + \mu)\nabla\nabla \cdot \boldsymbol{u} + \omega^2\boldsymbol{u} = 0 \quad \text{in} \quad \Omega, \tag{2.1}$$

together with the Dirichlet boundary condition

$$\boldsymbol{u} = 0 \quad \text{on} \quad \Gamma. \tag{2.2}$$

Given a curve $\Lambda \subset \mathbb{R}^2$ with the unit normal $\mathbf{n} = (n_1, n_2)^T \in \mathbb{S}$, the *generalised stress* operator $\boldsymbol{P}$ on $\Lambda$ is defined by

$$\boldsymbol{P}\boldsymbol{u} := (\mu + \tilde{\mu})\frac{\partial \boldsymbol{u}}{\partial \boldsymbol{n}} + \tilde{\lambda}\boldsymbol{n}\nabla \cdot \boldsymbol{u} - \tilde{\mu}\boldsymbol{n}^{\perp}\nabla^{\perp} \cdot \boldsymbol{u}, \quad \nabla^{\perp} := (-\partial_2, \partial_1).$$

Here, $\boldsymbol{n}^{\perp} = (-n_2, n_1)^T$ and $\tilde{\mu}, \tilde{\lambda}$ are real numbers satisfying $\tilde{\mu} + \tilde{\lambda} = \mu + \lambda$. A special choice of $\tilde{\mu}$ and $\tilde{\lambda}$ with $\tilde{\mu} = \mu(\mu + \lambda)/(3\mu + \lambda)$ and $\tilde{\lambda} = (2\mu + \lambda)(\mu + \lambda)/(3\mu + \lambda)$ will be used in this paper; see [4, chapter 3] for details.

Let $\Gamma_a := \{x = (x_1, x_2) \mid x_2 = a\}$ and $U_a := \{x = (x_1, x_2) \mid x_2 > a\}$. In this paper we require the scattered field $\boldsymbol{u}^{\mathrm{sc}} = \boldsymbol{u} - \boldsymbol{u}^{\mathrm{in}}$ to fulfill the *Upwards Propagating Radiation Condition (UPRC)* (see [5]):

$$\boldsymbol{u}^{\mathrm{sc}}(x) = \int_{\Gamma_a} \boldsymbol{P}_y[\Pi_a(x, y)]\phi(y)\mathrm{d}s(y), \quad x \in U_a \tag{2.3}$$

for some $a > f_+ := \sup_{x_1 \in \mathbb{R}} f(x_1)$ with some $\phi \in [L^{\infty}(\Gamma_a)]^2$. Here, $\Pi_a(x, y)$ denotes the Green's tensor for the *Navier* equation in the half plane $x_2 > a$ with the homogeneous Dirichlet

boundary condition on $\Gamma_a$. The differential operator $\boldsymbol{P}_y[\Pi_a(x,y)]$ is understood as the action of the *generalised stress* operator $\boldsymbol{P}$ to each column of $\Pi_a(x,y)$ with respect to the argument $y$. The explicit expression of $\Pi_a(x,y)$ can be found in [5] in two dimensions. Below we formulate the forward elastic scattering problem as a boundary value problem.

**Problem 2.1.** Given $\boldsymbol{g} \in [BC(\Gamma) \cap H^{1/2}_{\mathrm{loc}}(\Gamma)]^2$, find a vector field $\boldsymbol{u} \in [C^2(\Omega) \cap C(\overline{\Omega}) \cap H^1_{\mathrm{loc}}(\Omega)]^2$ that satisfies

1. the Navier equation (2.1) in $\Omega$,
2. the Dirichlet boundary condition $\boldsymbol{u} = \boldsymbol{g}$ on $\Gamma$,
3. the vertical growth rate condition: $\sup_{x\in\Omega} |x_2|^{\beta}|\boldsymbol{u}(x)| < \infty$ for some $\beta \in \mathbb{R}$ ,
4. the UPRC (2.3).

Well-posedness of the forward elastic scattering of plane waves in 2D was investigated in [4–6] using the integral equation method and in [18] using the variational approach in weighted Sobolev spaces. In particular, the unique solution to problem 2.1 can be written in the form of a combined single- and double-layer potential (see [5, 6])

$$\boldsymbol{u}(x) = \int_\Gamma \{\boldsymbol{P}_y[\Pi_h(x,y)] - \mathrm{i}\eta\Pi_h(x,y)\}\,\boldsymbol{\varphi}(y)\mathrm{d}s(y), \quad x \in \Omega,$$

where $h < \inf_{x_1\in\mathbb{R}} f(x_1)$, $\eta$ is a complex number satisfying $\Re(\eta) > 0$ and the density function $\boldsymbol{\varphi} \in [BC(\Gamma) \cap H^{1/2}_{\mathrm{loc}}(\Gamma)]^2$ is the unique solution to the boundary integral equation

$$(\boldsymbol{I} + \boldsymbol{D} - \mathrm{i}\eta\boldsymbol{S})\boldsymbol{\varphi}(y) = 2\boldsymbol{u}^{\mathrm{in}}(y), \quad y \in \Gamma.$$

Note that the boundary integral operators $\boldsymbol{S}$ and $\boldsymbol{D}$ are defined, respectively, as

$$\boldsymbol{S}\boldsymbol{\varphi}(y) := 2\int_\Gamma \Pi_h(y,\xi)\boldsymbol{\varphi}(\xi)\mathrm{d}\xi, \quad \boldsymbol{D}\boldsymbol{\varphi}(y) := 2\int_\Gamma \boldsymbol{P}_y[\Pi_h(y,\xi)]\boldsymbol{\varphi}(\xi)\mathrm{d}\xi.$$

It was verified in [6] that the operator $\boldsymbol{I} + \boldsymbol{D} - \mathrm{i}\eta\boldsymbol{S}$ is bijective on $[BC(\Gamma)]^2$. Further, it holds that

$$\|(\boldsymbol{I} + \boldsymbol{D} - \mathrm{i}\eta\boldsymbol{S})^{-1}\| < \infty.$$

We summarize the well-posedness of problem 2.1 in the following theorem.

**Theorem 2.2 (See [4, theorem 5.24]).** *For any Dirichlet data $\boldsymbol{g} \in [BC(\Gamma) \cap H^{1/2}_{\mathrm{loc}}(\Gamma)]^2$, there exists a unique solution $\boldsymbol{u} \in [C^2(\Omega) \cap C(\overline{\Omega}) \cap H^1_{\mathrm{loc}}(\Omega)]^2$ to problem 2.1, which depends continuously on $\|\boldsymbol{g}\|_{\infty;\Gamma}$, uniformly in $[C(\overline{\Omega} \setminus U_a)]^2$ for any $a > f_+$.*

## 3. Inverse scattering problem

### 3.1. Description of the imaging functional

Introduce the notation

$$\begin{aligned}
\Gamma_{a,A} &:= \{x \in \Omega \mid x_2 = a, |x_1| \leqslant A\},\ a > f_+,\\
\mathbb{S}_+ &:= \left\{\boldsymbol{d} = (d_1,d_2)^T \mid |\boldsymbol{d}| = 1, d_2 > 0\right\},\\
\mathbb{S}_- &:= \left\{\boldsymbol{d} = (d_1,d_2)^T \mid |\boldsymbol{d}| = 1, d_2 < 0\right\}.
\end{aligned}$$

The purpose of this section is to propose a non-iterative inversion scheme for determining $\Gamma$ from the scattered near-field data measured on $\Gamma_{a,A}$ excited by either compressional plane waves $\boldsymbol{u}_{\mathrm{p}}^{\mathrm{in}}(x;\boldsymbol{d})$, or shear plane waves $\boldsymbol{u}_{\mathrm{s}}^{\mathrm{in}}(x;\boldsymbol{d})$ or both of them.

We begin with the free-field Green's tensor $\Pi(x,y)$ for the two-dimensional *Navier* equation, given by

$$\Pi(x,z) := \frac{1}{\mu}\boldsymbol{I}\Phi_{k_{\mathrm{s}}}(x,z) + \frac{1}{\omega^2}\nabla_x^T\nabla_x\left(\Phi_{k_{\mathrm{s}}}(x,z) - \Phi_{k_{\mathrm{p}}}(x,z)\right), \tag{3.1}$$

with $x,z\in\mathbb{R}^2$ and $x\neq z$. Here, $\boldsymbol{I}$ denotes the 2-by-2 unit matrix and the scalar function $\Phi_k(x,z)$ is the fundamental solution to the two-dimensional *Helmholtz* equation given by

$$\Phi_k(x,z) = \frac{\mathrm{i}}{4}H_0^{(1)}(k|x-z|), \quad x\neq z, \tag{3.2}$$

where $H_0^{(1)} := J_0 + \mathrm{i}Y_0$ is the Hankel function of the first kind of order zero. The functions $J_n$ and $Y_n$ are the Bessel and Neumann functions of order $n$, respectively. To derive our indicator function, we recall the Funk–Hecke formula which is useful in simplifying calculations of certain integrals over the unit sphere; see, e.g. [13]). The original Funk–Hecke Formula (also known as the Hecke–Funk Formula, see [3, chapter 9, section 9.8]) basically allows one to calculate the convolution of a kernel function with a spherical function in a convenient way, which was first published by Funk in 1916 and then by Hecke in 1918.

**Lemma 3.1 (The Funk–Hecke formula, see, e.g. [13]).** *For any $k>0$, we have*

$$\frac{1}{2\pi}\int_{\mathbb{S}} \mathrm{e}^{\mathrm{i}k(x-z)\cdot\boldsymbol{d}}\mathrm{d}s(\boldsymbol{d}) = J_0(k|x-z|), \quad x,z\in\mathbb{R}^2.$$

Combining the above lemma with (3.2), we obtain

$$\mathrm{Im}\left(\Phi_k(x,z)\right) = \frac{1}{4}J_0(k|x-z|) = \frac{1}{8\pi}\int_{\mathbb{S}}\mathrm{e}^{\mathrm{i}k(x-z)\cdot\boldsymbol{d}}\mathrm{d}s(\boldsymbol{d}). \tag{3.3}$$

Taking the imaginary part of (3.1) and using (3.3) yield

$$\mathrm{Im}\,\Pi(x,z) = \frac{1}{8\pi}\left[\frac{1}{\lambda+2\mu}\int_{\mathbb{S}}\boldsymbol{d}\otimes\boldsymbol{d}\mathrm{e}^{\mathrm{i}k_{\mathrm{p}}(x-z)\cdot\boldsymbol{d}}\mathrm{d}s(\boldsymbol{d}) + \frac{1}{\mu}\int_{\mathbb{S}}(\boldsymbol{I}-\boldsymbol{d}\otimes\boldsymbol{d})\mathrm{e}^{\mathrm{i}k_{\mathrm{s}}(x-z)\cdot\boldsymbol{d}}\mathrm{d}s(\boldsymbol{d})\right], \tag{3.4}$$

where

$$\boldsymbol{d}\otimes\boldsymbol{d} := \boldsymbol{d}\boldsymbol{d}^T = \begin{bmatrix} d_1^2 & d_1d_2 \\ d_2d_1 & d_2^2\end{bmatrix}, \quad \boldsymbol{d} = (d_1,d_2)^T\in\mathbb{S}.$$

Set $\boldsymbol{e}_1 = (1,0)^T$ and $\boldsymbol{e}_2 = (0,1)^T$. Then, for $j=1,2$,

$$\mathrm{Im}(\Pi(x,z)\boldsymbol{e}_j) = \frac{1}{8\pi}\left[\frac{1}{\lambda+2\mu}\int_{\mathbb{S}}d_j\boldsymbol{d}\mathrm{e}^{\mathrm{i}k_{\mathrm{p}}(x-z)\cdot\boldsymbol{d}}\mathrm{d}s(\boldsymbol{d}) + \frac{1}{\mu}\int_{\mathbb{S}}d_j^{\perp}\boldsymbol{d}^{\perp}\mathrm{e}^{\mathrm{i}k_{\mathrm{s}}(x-z)\cdot\boldsymbol{d}}\mathrm{d}s(\boldsymbol{d})\right], \tag{3.5}$$

where $d_j^{\perp}$ stands for the $j$th component of $\boldsymbol{d}^{\perp}$, that is, $d_1^{\perp} = -d_2$, $d_2^{\perp} = d_1$.

**Lemma 3.2.** *For $\boldsymbol{d}\in\overline{\mathbb{S}}_+$, the scattered fields corresponding to the incident plane waves $\boldsymbol{u}_{\mathrm{p}}^{\mathrm{in}}(x;\boldsymbol{d})$ and $\boldsymbol{u}_{\mathrm{s}}^{\mathrm{in}}(x;\boldsymbol{d})$ are given as $\boldsymbol{u}_{\mathrm{p}}^{\mathrm{sc}}(x;\boldsymbol{d}) := -\boldsymbol{d}\mathrm{e}^{\mathrm{i}k_{\mathrm{p}}x\cdot\boldsymbol{d}}$ and $\boldsymbol{u}_{\mathrm{s}}^{\mathrm{sc}}(x;\boldsymbol{d}) := -\boldsymbol{d}^{\perp}\mathrm{e}^{\mathrm{i}k_{\mathrm{s}}x\cdot\boldsymbol{d}}$, $x\in\Omega$, respectively.*

**Proof.** It is easily seen that $\boldsymbol{u}_{\mathrm{p}}^{\mathrm{sc}}(x;\boldsymbol{d})$ satisfies the *Navier* equation (2.1) and the vertical growth rate condition defined in problem 2.1. Since $\boldsymbol{u}_{\mathrm{p}}^{\mathrm{sc}}(x;\boldsymbol{d})$ is upward propagating for $\boldsymbol{d}\in\overline{\mathbb{S}}_+$, it satisfies the UPRC in (2.3); see [4, remark 2.14]. Further, we have the boundary data $\boldsymbol{u}_{\mathrm{p}}^{\mathrm{sc}}(x;\boldsymbol{d})=-\boldsymbol{u}_{\mathrm{p}}^{\mathrm{in}}(x;\boldsymbol{d})$ on $\Gamma$. By the uniqueness of solutions to the forward scattering problem (see theorem 2.2), we conclude that the function $\boldsymbol{u}_{\mathrm{p}}^{\mathrm{sc}}(x;\boldsymbol{d}):=-\boldsymbol{d}\mathrm{e}^{\mathrm{i}k_{\mathrm{p}}x\cdot\boldsymbol{d}}$, $x\in\Omega$, is the unique scattered field corresponding to the incident plane wave $\boldsymbol{u}_{\mathrm{p}}^{\mathrm{in}}(x;\boldsymbol{d})$. The shear wave case can be proved similarly. □

Denote by $\boldsymbol{u}_{\mathrm{p}}^{\mathrm{sc}}(x;\boldsymbol{d})$, $\boldsymbol{u}_{\mathrm{s}}^{\mathrm{sc}}(x;\boldsymbol{d})\in[C^2(\Omega)\cap C(\overline{\Omega})\cap H^1_{\mathrm{loc}}(\Omega)]^2$ the unique outgoing scattered field (see theorem 2.2) corresponding to the incident plane compressional wave $\boldsymbol{u}_{\mathrm{p}}^{\mathrm{in}}(x;\boldsymbol{d})$ and plane shear waves $\boldsymbol{u}_{\mathrm{s}}^{\mathrm{in}}(x;\boldsymbol{d})$ with $\boldsymbol{d}\in\mathbb{S}_-$, respectively. Our imaging functional will depend on the measurement data $\boldsymbol{u}_{\mathrm{p}}^{\mathrm{sc}}(x;\boldsymbol{d})$, $\boldsymbol{u}_{\mathrm{s}}^{\mathrm{sc}}(x;\boldsymbol{d})$ for $x\in\Gamma_a$ and $\boldsymbol{d}\in\mathbb{S}_-$. Recalling the free-field's Green's tensor $\Pi$ (see (3.1)), we introduce a new function

$$\boldsymbol{U}^{\mathrm{in}}(x;z,\boldsymbol{e}_j):=\mathrm{Im}\,(\Pi(x,z)\boldsymbol{e}_j),\quad j=1,2, \tag{3.6}$$

for $x,z\in\Omega$, $x\neq z$, which can be mathematically regarded as an incident wave onto the surface $\Gamma$. $U^{\mathrm{in}}$ is mathematically meaningful only, since by (3.5) it consists of both downward and upward propagating plane waves. Such kind of incoming waves may help design our imaging function, but they are not experimental incident fields. Next we shall express the scattered field excited by $\boldsymbol{U}^{\mathrm{in}}(x;z,\boldsymbol{e}_j)$, which we denote by $\boldsymbol{U}^{\mathrm{sc}}(x;z,\mathbf{e}_j)$, in terms of the scattered fields $\boldsymbol{u}_{\mathrm{p}}^{\mathrm{sc}}$ and $\boldsymbol{u}_{\mathrm{s}}^{\mathrm{sc}}$.

**Theorem 3.3.** *The scattered field generated by* $\boldsymbol{U}^{\mathrm{in}}(x;z,\boldsymbol{e}_j)$ *takes the form*

$$\begin{aligned}\boldsymbol{U}^{\mathrm{sc}}(x;z,\mathbf{e}_j)=&\frac{1}{8\pi}\left[\frac{1}{\lambda+2\mu}\int_{\mathbb{S}_-}\boldsymbol{u}_{\mathrm{p}}^{\mathrm{sc}}(x;\boldsymbol{d})d_j\mathrm{e}^{-\mathrm{i}k_pz\cdot\boldsymbol{d}}\mathrm{d}s(\boldsymbol{d})+\frac{1}{\mu}\int_{\mathbb{S}_-}\boldsymbol{u}_{\mathrm{s}}^{\mathrm{sc}}(x;\boldsymbol{d})d_j^{\perp}\mathrm{e}^{-\mathrm{i}k_s\mathbf{z}\cdot\boldsymbol{d}}\mathrm{d}s(\boldsymbol{d})\right]\\&-\frac{1}{8\pi}\left[\frac{1}{\lambda+2\mu}\int_{\mathbb{S}_-}d_j'\boldsymbol{d}'\mathrm{e}^{\mathrm{i}k_{\mathrm{p}}(x'-z')\cdot\boldsymbol{d}}\mathrm{d}s(\boldsymbol{d})+\frac{1}{\mu}\int_{\mathbb{S}_-}(d')_j^{\perp}(\boldsymbol{d}')^{\perp}\mathrm{e}^{\mathrm{i}k_{\mathrm{s}}(x'-z')\cdot\boldsymbol{d}}\mathrm{d}s(\boldsymbol{d})\right].\end{aligned} \tag{3.7}$$

*Here,* $x'=(x_1,-x_2)$ *for* $x=(x_1,x_2)\in\mathbb{R}^2$. *The notation* $d_j'$ *and* $(d')_j^{\perp}$ *denote the jth component of* $\boldsymbol{d}'$ *and* $(\boldsymbol{d}')^{\perp}$, *respectively, given by*

$$d_1'=d_1,\quad d_2'=-d_2,\quad (d')_1^{\perp}=d_2,\quad (d')_2^{\perp}=d_1.$$

**Proof.** In view of (3.5), the incident field $\boldsymbol{U}^{\mathrm{in}}(x;z,\boldsymbol{e}_j)$ can be decomposed into the sum of four parts:

$$\boldsymbol{U}^{\mathrm{in}}=\frac{1}{8\pi}\left\{\frac{1}{\lambda+2\mu}(\boldsymbol{U}_{p,-}^{\mathrm{in}}+\boldsymbol{U}_{p,+}^{\mathrm{in}})+\frac{1}{\mu}(\boldsymbol{U}_{s,+}^{\mathrm{in}}+\boldsymbol{U}_{s,-}^{\mathrm{in}})\right\},$$

where

$$\begin{aligned}\boldsymbol{U}_{p,\pm}^{\mathrm{in}}(x;z,\boldsymbol{e}_j):&=\int_{\mathbb{S}_\pm}\boldsymbol{u}_{\mathrm{p}}^{\mathrm{in}}(x;\boldsymbol{d})d_j\mathrm{e}^{-\mathrm{i}k_pz\cdot\boldsymbol{d}}\mathrm{d}s(\boldsymbol{d})=\int_{\mathbb{S}_\pm}\boldsymbol{d}d_j\mathrm{e}^{\mathrm{i}k_{\mathrm{p}}(x-z)\cdot\boldsymbol{d}}\mathrm{d}s(\boldsymbol{d}),\\\boldsymbol{U}_{s,\pm}^{\mathrm{in}}(x;z,\boldsymbol{e}_j):&=\int_{\mathbb{S}_\pm}\boldsymbol{u}_{\mathrm{s}}^{\mathrm{in}}(x;\boldsymbol{d})d_j^{\perp}\mathrm{e}^{-\mathrm{i}k_sz\cdot\boldsymbol{d}}\mathrm{d}s(\boldsymbol{d})=\int_{\mathbb{S}_\pm}\boldsymbol{d}^{\perp}d_j^{\perp}\mathrm{e}^{\mathrm{i}k_s(x-z)\cdot\boldsymbol{d}}\mathrm{d}s(\boldsymbol{d}).\end{aligned}$$

By linear superposition and lemma 3.2, the unique scattered field $\boldsymbol{U}^{\mathrm{sc}}_{p,+}$ that corresponds to $\boldsymbol{U}^{\mathrm{in}}_{p,+}$ is given by

$$\boldsymbol{U}^{\mathrm{sc}}_{p,+}(x;z,\boldsymbol{e}_j) := \int_{\mathbb{S}_+} \boldsymbol{u}^{\mathrm{sc}}_{\mathrm{p}}(x;\boldsymbol{d}) d_j \mathrm{e}^{-\mathrm{i}k_p z\cdot\boldsymbol{d}} \mathrm{d}s(\boldsymbol{d}) = -\int_{\mathbb{S}_+} \boldsymbol{d}\, d_j \mathrm{e}^{\mathrm{i}k_{\mathrm{p}}(x-z)\cdot\boldsymbol{d}} \mathrm{d}s(\boldsymbol{d}),$$

implying that

$$\boldsymbol{U}^{\mathrm{sc}}_{p,+}(x;z,\boldsymbol{e}_j) = -\boldsymbol{U}^{\mathrm{in}}_{p,+}(x;z,\boldsymbol{e}_j) = -\int_{\mathbb{S}_-} d'_j \boldsymbol{d}' \mathrm{e}^{\mathrm{i}k_{\mathrm{p}}(x'-z')\cdot\boldsymbol{d}} \mathrm{d}s(\boldsymbol{d}).$$

Analogously, we have

$$\boldsymbol{U}^{\mathrm{sc}}_{s,+}(x;z,\boldsymbol{e}_j) = -\boldsymbol{U}^{\mathrm{in}}_{s,+}(x;z,\boldsymbol{e}_j) = \int_{\mathbb{S}_-} (d')^{\perp}_j (\boldsymbol{d}')^{\perp} \mathrm{e}^{\mathrm{i}k_{\mathrm{s}}(x'-z')\cdot\boldsymbol{d}} \mathrm{d}s(\boldsymbol{d}).$$

On the other hands, it is easy to see that the unique scattered fields excited by $\boldsymbol{U}^{\mathrm{in}}_{p,-}$ and $\boldsymbol{U}^{\mathrm{in}}_{s,-}$ can be expressed as

$$\boldsymbol{U}^{\mathrm{sc}}_{p,-}(x;z,\boldsymbol{e}_j) := \int_{\mathbb{S}_-} \boldsymbol{u}^{\mathrm{sc}}_{\mathrm{p}}(x;\boldsymbol{d}) d_j \mathrm{e}^{-\mathrm{i}k_p z\cdot\boldsymbol{d}} \mathrm{d}s(\boldsymbol{d}),$$
$$\boldsymbol{U}^{\mathrm{sc}}_{s,-}(x;z,\boldsymbol{e}_j) := \int_{\mathbb{S}_-} \boldsymbol{u}^{\mathrm{sc}}_{\mathrm{s}}(x;\boldsymbol{d}) d_j \mathrm{e}^{-\mathrm{i}k_s z\cdot\boldsymbol{d}} \mathrm{d}s(\boldsymbol{d}),$$

respectively. To sum up, we may rewrite the scattered field excited by $\boldsymbol{U}^{\mathrm{in}}$ as

$$\boldsymbol{U}^{\mathrm{sc}} = \frac{1}{8\pi}\left\{\frac{1}{\lambda+2\mu}(\boldsymbol{U}^{\mathrm{sc}}_{p,-}+\boldsymbol{U}^{\mathrm{sc}}_{p,+}) + \frac{1}{\mu}(\boldsymbol{U}^{\mathrm{sc}}_{s,+}+\boldsymbol{U}^{\mathrm{sc}}_{s,-})\right\},$$

which takes the same form as the right-hand side of (3.7). The proof is thus completed. □

**Remark 3.4.**

(i) For $j = 1, 2$, it follows from (3.5) that $\boldsymbol{U}^{\mathrm{in}}(x;z,\boldsymbol{e}_j)$ can be divided into the compressional part $\boldsymbol{U}^{\mathrm{in}}_{\mathrm{p}}(x;z,\boldsymbol{e}_j)$ and the shear part $\boldsymbol{U}^{\mathrm{in}}_{\mathrm{s}}(x;z,\boldsymbol{e}_j)$, that is, $\boldsymbol{U}^{\mathrm{in}}(x;z,\boldsymbol{e}_j) = \boldsymbol{U}^{\mathrm{in}}_{\mathrm{p}}(x;z,\boldsymbol{e}_j) + \boldsymbol{U}^{\mathrm{in}}_{\mathrm{s}}(x;z,\boldsymbol{e}_j)$, where

$$\boldsymbol{U}^{\mathrm{in}}_{\mathrm{p}}(x;z,\boldsymbol{e}_j) := \left(-\frac{1}{\omega^2}\nabla^T_x \nabla_x \mathrm{Im}\, G_{k_{\mathrm{p}}}(x,z)\right) e_j,$$
$$\boldsymbol{U}^{\mathrm{in}}_{\mathrm{s}}(x;z,\boldsymbol{e}_j) := \left(\frac{1}{\mu} I + \frac{1}{\omega^2}\nabla^T_x \nabla_x \mathrm{Im}\, G_{k_{\mathrm{s}}}(x,z)\right) e_j.$$

Then, similarly as in the proof of the above theorem, it can be proved that the scattered fields generated by $\boldsymbol{U}^{\mathrm{in}}_{\mathrm{p}}(x;z,\boldsymbol{e}_j)$ and $\boldsymbol{U}^{\mathrm{in}}_{\mathrm{s}}(x;z,\boldsymbol{e}_j)$ take the form

$$\boldsymbol{U}^{\mathrm{sc}}_{\mathrm{p}}(x;z,\boldsymbol{e}_j) = \frac{1}{8\pi(\lambda+2\mu)}\int_{\mathbb{S}_-}\left(\boldsymbol{u}^{\mathrm{sc}}_{\mathrm{p}}(x;\boldsymbol{d}) d_j \mathrm{e}^{-\mathrm{i}k_p z\cdot\boldsymbol{d}} - d'_j \boldsymbol{d}' \mathrm{e}^{\mathrm{i}k_{\mathrm{p}}(x'-z')\cdot\boldsymbol{d}}\right) \mathrm{d}s(\boldsymbol{d})$$

and

$$\boldsymbol{U}_{\mathrm{s}}^{\mathrm{sc}}(x;z,\mathbf{e}_j)=\frac{1}{8\pi\mu}\int_{\mathbb{S}_-}\left(\boldsymbol{u}_{\mathrm{s}}^{\mathrm{sc}}(x;\boldsymbol{d})d_j^{\perp}\mathrm{e}^{-\mathrm{i}k_{\mathrm{s}}\mathbf{z}\cdot\boldsymbol{d}}-(d')_j^{\perp}(\boldsymbol{d}')^{\perp}\mathrm{e}^{\mathrm{i}k_{\mathrm{s}}(x'-z')\cdot\boldsymbol{d}}\right)\mathrm{d}s(\boldsymbol{d}),$$

respectively. The above formulas will be used in the numerical example when we only consider incident compressional plane wave or incident shear plane wave.

(ii) Our inversion scheme requires knowledge of the total (scattered) field separately excited by incident compressional and shear plane waves from the upper half plane. However, our approach does not work in the case that the incident wave is a linear combination of compressional and shear plane waves, due to formulas (3.4) and (3.5).

From the proof of theorem 2.2 (see [4]), we can represent $\boldsymbol{U}^{\mathrm{sc}}(x;z,\boldsymbol{e}_j)$ in (3.7) as the layer-potential

$$\boldsymbol{U}^{\mathrm{sc}}(x;z,\boldsymbol{e}_j)=\int_{\Gamma}\{\boldsymbol{P}_y[\Pi_h(x,y)]-\mathrm{i}\eta\boldsymbol{\Pi}_h(x,y)\}\,\boldsymbol{\psi}_z^{(j)}(y)\mathrm{d}s(y),\quad x\in\Omega,\tag{3.8}$$

where the density function $\boldsymbol{\psi}_z^{(j)}$ is the unique solution to the integral equation

$$(\boldsymbol{I}+\boldsymbol{D}-\mathrm{i}\eta\boldsymbol{S})\boldsymbol{\psi}_z^{(j)}=-2\boldsymbol{G}_z^{(j)}\quad\text{on}\quad\Gamma,$$

with

$$\boldsymbol{G}_z^{(j)}(x):=-\boldsymbol{U}^{\mathrm{in}}(x;z,\boldsymbol{e}_j)=-\mathrm{Im}\;\Pi(x;z)\boldsymbol{e}_j.$$

Here, we use the subscript $z$ to indicate the dependence of $\psi_z^{(j)}$ on the point $z$. By (3.1) and a straightforward calculation it follows that

$$\mathrm{Im}[\Pi_{j,k}(x,z)]=\frac{1}{4\mu}\left[F_1(|x-z|)\,\delta_{j,k}+F_2(|x-z|)\,\frac{(x_j-z_j)(x_k-z_k)}{|x-z|^2}\right],\tag{3.9}$$

where

$$F_1(t)=J_0(k_st)-\frac{1}{k_st}\left(J_1(k_st)-\frac{k_{\mathrm{p}}}{k_{\mathrm{s}}}\,J_1(k_pt)\right),$$
$$F_2(t)=\frac{2}{k_st}J_1(k_st)-J_0(k_st)-\frac{k_{\mathrm{p}}}{t}J_1(k_pt)+\frac{k_{\mathrm{p}}^2}{k_{\mathrm{s}}^2}J_0(k_pt).$$

We remark that the Bessel functions have the following behavior [13, section 2.4] (see also figure 2)

$$J_n(t)=\sum_{p=0}^{\infty}\frac{(-1)^p}{p!(n+p)!}\left(\frac{t}{2}\right)^{n+2p},\quad t\in\mathbb{R}.$$

For large arguments, it holds that

$$J_n(t)=\sqrt{\frac{2}{\pi t}}\cos\left(t-\frac{n\pi}{2}-\frac{\pi}{4}\right)\left\{1+O\left(\frac{1}{t}\right)\right\},\quad t\to\infty.$$

Thus, from the expression of $\mathrm{Im}[\Pi(x,z)]$ in (3.9) we have the estimate

$$\max_{j,k=1,2}|\mathrm{Im}\Pi_{jk}(x,z)|=\begin{cases}O(1) & \text{as } |x-z|\to 0,\\ O\left(|x-z|^{-1/2}\right) & \text{if } |x-z|\to\infty,\end{cases}\quad x\in\Gamma.$$

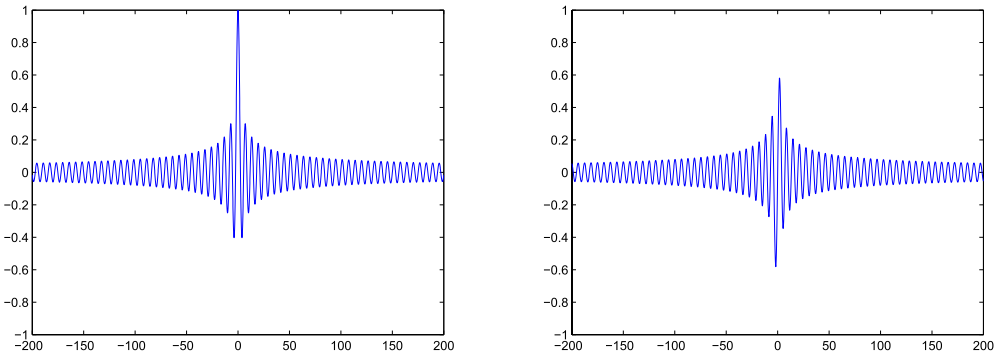

**Figure 2.** The behavior of the Bessel functions $J_0$ (left) and $J_1$ (right).

Further, since $\boldsymbol{I}+\boldsymbol{D}-\mathrm{i}\eta\boldsymbol{S}$ is bijective (and so boundedly invertible) in $[BC(\Gamma)]^2$, it holds that

$$C_1\|\boldsymbol{G}_z^{(j)}\|_{\infty,\Gamma}\leqslant\|\boldsymbol{\psi}_z^{(j)}\|_{\infty,\Gamma}\leqslant C_2\|\boldsymbol{G}_z^{(j)}\|_{\infty,\Gamma},\quad j=1,2 \tag{3.10}$$

for some positive constants $C_1$ and $C_2$. By (3.10) we have

$$\begin{cases}\|\boldsymbol{\psi}_z^{(j)}\|_{\infty,\Gamma}\geqslant C>0 & \text{if } \operatorname{dist}(z,\Gamma)\to 0,\\ \|\boldsymbol{\psi}_z^{(j)}\|_{\infty,\Gamma}=O\left(d(\mathbf{z},\Gamma)^{-1/2}\right) & \text{as } \operatorname{dist}(z,\Gamma)\to\infty,\end{cases}\quad j=1,2.$$

Combining the above estimate with (3.8), we expect that the scattered field $\boldsymbol{U}^{\mathrm{sc}}(x;z,\boldsymbol{e}_j)$ for $x\in\Omega$ takes a relatively large value when the sampling point $z$ is getting close to the rough surface $\Gamma$ and decays with the order $1/\operatorname{dist}(z,\Gamma)^{1/2}$ as $z$ moves away from the rough surface $\Gamma$. Motivated by the above discussions, we propose the imaging function

$$I(z):=\sum_{j=1}^{2}\int_{\Gamma_a}\left|\boldsymbol{U}^{\mathrm{sc}}(x;z,\boldsymbol{e}_j)\right|^2\mathrm{d}s(x), \tag{3.11}$$

for some $a>f^+$, where $\boldsymbol{U}^{\mathrm{sc}}$ is of the form (3.7) and $z\in\mathbb{R}^2$ is the sampling point in a searching region. Analogously, it is reasonable to expect that the imaging function $I(z)$ decays as $z$ moves away from the rough surface $\Gamma$. Hence, $I(z)$ can be regarded as an imaging function for recovering $\Gamma$.

In our numerical computations, the straight line $\Gamma_a$ in (3.11) is truncated by a finite line segment $\Gamma_{a,A}:=\{x\in\Gamma_a\mid|x_1|<A\}$, which will be discretized uniformly into $2N$ subintervals with the step size $h=A/N$. In addition, the lower-half circle $\mathbb{S}_-$ in (3.7) will also be uniformly discretized into $M$ grids with the step size $\Delta\theta=\pi/M$. Then for each sampling point $z$ we get the discrete form of (3.11) as follows:

$$\begin{aligned}I(z)\approx I_A(z)=\sum_{j=1}^{2}\Bigg|h\sum_{i=0}^{2N}\frac{\Delta\theta}{8\pi}\sum_{k=0}^{M}\Bigg(&\frac{1}{\lambda+2\mu}\boldsymbol{u}_{\mathrm{p}}^{sc}(x_i;\boldsymbol{d}_k)d_j\mathrm{e}^{-\mathrm{i}k_pz\cdot\boldsymbol{d}_k}+\frac{1}{\mu}\boldsymbol{u}_{\mathrm{s}}^{sc}(x_i;\boldsymbol{d}_k)d_j^{\perp}\mathrm{e}^{-\mathrm{i}k_sz\cdot\boldsymbol{d}_k}\\&-\frac{1}{\lambda+2\mu}(d_k)_j'\boldsymbol{d}_k'\mathrm{e}^{\mathrm{i}k_{\mathrm{p}}(x_i'-z')\cdot\boldsymbol{d}_k}-\frac{1}{\mu}(d_k')_j^{\perp}(\boldsymbol{d}_k')^{\perp}\mathrm{e}^{\mathrm{i}k_{\mathrm{s}}(x_i'-z')\cdot\boldsymbol{d}_k}\Bigg)\Bigg|^2.\end{aligned} \tag{3.12}$$

Here, the measurement positions are denoted by $x_i=(-A+ih,H)$ for $i=0,1,...,2N$, and the incident directions $\boldsymbol{d}_k=(\sin(-\pi+k\Delta\theta),\cos(-\pi+k\Delta\theta))$, $k=0,1,\cdots,M$. We note that the number $\Delta\theta$ gives arise to the discretized error for evaluating the integrals involved in (3.3), which is independent of $a$, $A$ and the sampling point $z$. Let $K\subset\mathbb{R}^2$ be a sampling region

which contains part of the rough surface to be recovered. Our imaging scheme (3.12) can be implemented as follows.

**Algorithm 3.1.**

1. Choose $\mathcal{T}$ to be a mesh of $K$ and choose $\Gamma_{a,A}$ ($a > f_+$) to be a straight line segment above the rough surface.
2. Collect the scattered near-field data $\boldsymbol{u}_{\mathrm{p}}^{\mathrm{sc}}(x_j;\boldsymbol{d}_k)$ and $\boldsymbol{u}_{\mathrm{s}}^{\mathrm{sc}}(x_j;\boldsymbol{d}_k)$ for $x_j \in \Gamma_{a,A}$, $j = 0, \cdots, 2N$, corresponding to the incident plane waves $\boldsymbol{u}_{\mathrm{p}}^{\mathrm{in}}(x;\boldsymbol{d}_k)$ and $\boldsymbol{u}_{\mathrm{s}}^{\mathrm{in}}(x;\boldsymbol{d}_k)$ with $k = 0, \cdots, M$, respectively.
3. For each sampling point $z \in \mathcal{T}$, compute the imaging function $I(z)$ by using (3.12).
4. Plot the imaging function $I(z)$ for $z \in \mathcal{T}$, where the large values represent the part of the rough surface in the sampling region $K$.

**Remark 3.5.**

1. It follows from (3.7) and (3.11) that our imaging functional requires the data $\boldsymbol{u}_{\mathrm{p}}^{\mathrm{sc}}(x;\boldsymbol{d})$ and $\boldsymbol{u}_{\mathrm{s}}^{\mathrm{sc}}(x;\boldsymbol{d})$ for incident compressional and shear plane waves with different directions, separately.
2. $\Gamma_a$ can be replaced by a curve or a set of random points. Numerical experiments will be reported in example 1 of section 4.

### *3.2. Comparison with other sampling schemes*

Recently, the linear sampling method, originally proposed by Colton and Kirsch in 1996 [14] for imaging bounded scatterers, was applied to inverse acoustic scattering from a locally perturbed sound-soft rough surface; see [15]. Being different from the case with bounded obstacles, near-field measurement data excited by point source waves were utilized and the following modified near-field equation was considered:

$$\int_{\Gamma_{a,A}} \left(u^{\mathrm{sc}}(x;y) - u^{\mathrm{re}}(x;y)\right) g_z(y)\,\mathrm{d}s(y) = u^{\mathrm{re}}(x;z) + \Phi_k(x,z), \quad x \in \Gamma_{a,A},$$

where $\Phi_k(\cdot,z)$ is the free-space Green's function to the Helmholtz equation with the wave-number $k^2$ (see (3.2)), $u^{\mathrm{sc}}(\cdot;y)$ is the scattered field excited by the incoming wave $\Phi_k(\cdot;y)$ and $u^{\mathrm{re}}(\cdot;y)$ is some 'artificial' reference field depending on $y \in \Gamma_{a,A}$. The indicator functional proposed by [15] seeks to plot the function $z \to ||g_z||_{L^2(\Gamma_{a,A})}$, where $g_z$ is a solution to the above modified near-field equation. It was proved in [15] that this imaging functional has a larger value for $z \in \Omega$ than those sampling points lying below $\Gamma$. In comparison with the scheme of [15], our inversion scheme is totally 'direct', because we do not need to solve any near-field equation. Moreover, our approach has been designed for imaging globally rough surfaces, which covers the case studied in [15]. We refer to [30] for the acoustic version of our approach.

Over the last few years, the topological derivative of data misfit cost functionals has been proposed as a new approach to inverse scattering; see [9, 10, 19]. The TS indicator quantifies the leading order perturbation of a given misfit functional when a trial obstacle is introduced in a fixed reference domain, leading to robust imaging functionals. In the frequency domain, the method of topological sensitivity has been so far applied to finding unknown scatterers of finite size from far-field patterns over all incident directions. The TS indicator functional can

be equivalently recast as (see [7, proposition 1] for inverse acoustic scattering from a bounded penetrable scatterer)

$$\tilde{T}(z) = \mathrm{Re} \int_{\mathbb{S}} \mathrm{e}^{-\mathrm{i}k\hat{x}\cdot z} \overline{\int_{\mathbb{S}} u^{\infty}(\hat{x};\boldsymbol{d})\mathrm{e}^{-\mathrm{i}k\boldsymbol{d}\cdot z}\mathrm{d}s(\boldsymbol{d})}\,\mathrm{d}s(\hat{x}).$$

Our imaging functional in the acoustic far-field case takes the form (see also [29])

$$I_F(z) = \int_{\mathbb{S}} \Big| \int_{\mathbb{S}} u^{\infty}(\hat{x};\boldsymbol{d})\mathrm{e}^{-\mathrm{i}k\boldsymbol{d}\cdot z}\mathrm{d}s(\boldsymbol{d})\Big|^2 \mathrm{d}s(\hat{x}),$$

which differs slightly from the TS indicator. To the best of our knowledge, the application of the TS indicator to inverse scattering from unbounded surfaces with near-field data is not available in the literature. As can be seen from (3.7), our indicator functional for half-space inverse problems consists of two part: the first line in (3.7) involves the near-field data in experiments, whereas the second line corrects the integrals in the first line so that $\boldsymbol{U}^{\mathrm{sc}}$ coincides with the scattered field excited by $\boldsymbol{U}^{\mathrm{in}}$.

It should be mentioned that a rigorous mathematical justification of our scheme seems still open. Hence, the characterization of the scattering surface provided by our method is not backed (for the time being) by mathematical proofs. We have rigorously justified the smallness of the imaging function away from the surface. However, it is still unclear why the imaging function peaks near the surface. As to the topological sensitivity method, although it has not yet been applied to the characterization of unbounded surfaces, there is no major theoretical obstacle to do so. Besides, [1, 2, 7, 20] have provided rigorous mathematical justifications for TS imaging functionals in some particular cases.

## 4. Numerical examples

In this section, we present several numerical experiments to demonstrate the effectiveness of our imaging method and investigate the specificities of elastic scattering problems. Emphasis will be placed upon the sensitivity of our inversion scheme to the parameters involved, such as noise levels, positions of measurements, incident frequencies, height and length of the measurement line segment and numbers of incident plane waves and measurement points. To highlight the differences between the elastic case and the acoustic case, we will investigate the influence of Lamé constants, polarization directions, types of incident waves and partial near-field elastic measurements on the reconstructed results. We use the Nyström method to solve the forward elastic scattering problem for a rigid rough surface [25, 26]. The scattered near-field data will be polluted by

$$\boldsymbol{u}^{\mathrm{sc}}_{\delta}(x) = \boldsymbol{u}^{\mathrm{sc}}(x) + \delta(\zeta_1 + i\zeta_2)\max_x |\boldsymbol{u}^{\mathrm{sc}}(x)|,$$

where $\delta$ is the noise level and $\zeta_1, \zeta_2$ are standard normal distributions. If not stated otherwise, we make the following assumptions:

1. We choose $N = 201$, $M = 256$, $\delta = 20\%$.
2. The scattered near-field data is measured on the straight line $\Gamma_{a,A}$ with $a = 2, A = 8$.
3. The sampling region will be set to be a rectangular domain.
4. The Lamé constants are taken as $\mu = 1, \lambda = 1$ and the frequency is taken as $\omega = 20$.

In some of our experiments, the above mentioned parameters will also be changed to investigate their effect on the reconstructed results. In each figure, we use a solid line to represent the actual rough surface against the reconstructed one.

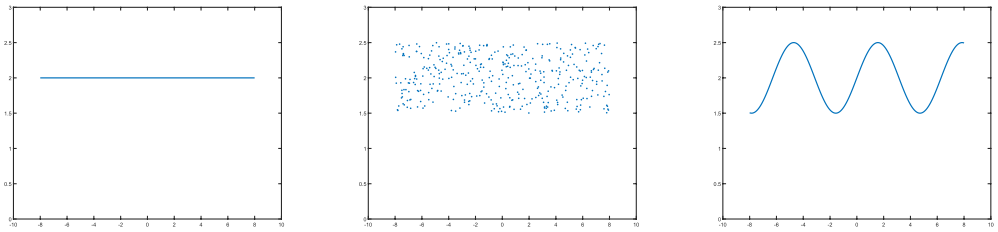

(a) (b) (c)

**Figure 3.** The profiles of different positions of measurements. (a) $\Gamma_1^{\text{mea}}$: straight line. (b) $\Gamma_2^{\text{mea}}$: random points. (c) $\Gamma_3^{\text{mea}}$: curve.

**Example 1.** In this example, we will study the influence of different measurement positions on the reconstructed results. We consider three kinds of positions of measurements which are denoted as $\Gamma_i^{\text{mea}}, i = 1, 2, 3$, respectively. Here, $\Gamma_1^{\text{mea}}$ is chosen to be the straight line $\Gamma_{a,A}$ that used in the above assumptions, $\Gamma_2^{\text{mea}}$ is composed of random points in the region $[-8, 8] \times [1.5, 2.5]$ and $\Gamma_3^{\text{mea}} = \{(x_1, \sin x_1) \mid x_1 \in [-8, 8]\}$ is a finite curve. The profiles of $\Gamma_i^{\text{mea}}$ $(i = 1, 2, 3)$ are presented in figure 3. For each case, the number of measurement points is chosen to be the same as in the above assumptions. We consider the rough surface $\Gamma$ with

$$f(x_1) = \begin{cases} 0.42 - 0.1\cos(0.75x_1) - 0.05\cos(7x_1) & x_1 < 4, \\ 0.55 & \text{else.} \end{cases} \tag{4.1}$$

Figure 4 presents the reconstructed results of the imaging function $I(z)$ with the positions of measurements $\Gamma_i^{\text{mea}}$ $(i = 1, 2, 3)$, from the exact, 20% noisy and 40% noisy data. Here, for all cases, we just use (3.12) with $A = 8$ to compute the imaging function $I(z)$. It is shown in figure 4 that the proposed scheme is robust to noise, even at the level of 40% noise. Further, it can be seen that our inversion algorithm works well for different kinds of measurement positions. Therefore, for simplicity, we only suppose the positions of measurements to be a finite line segment in the remaining examples.

**Example 2.** We will study the influence of incident frequencies on the reconstructed results. We assume that the rough surface $\Gamma$ is given by (4.1). Figure 5 presents the reconstructed results of the imaging function $I(z)$ from the data at the incident frequencies $\omega = 5, 15, 25$, respectively. It can be seen that the imaging result with lower frequency $\omega = 5$ can only capture the macro-scale features of the rough surface, while the use of the higher frequency data at $\omega = 25$ can capture not only the micro-scale but also the macro-scale features.

**Example 3.** In this example, we consider the influence of the measurement surface $\Gamma_{a,A}$ with different parameters $a$ and $A$ on the reconstructed results. Note that $a$ and $2A$ denote the height and length of the line segment $\Gamma_{a,A}$, respectively. We consider the original rough surface $\Gamma$ with

$$f(x_1) = 0.5 + 0.14\sin(0.7\pi(x_1 + 0.6)).$$

Figures 6(a)–(c) present the reconstructed results of the imaging function $I(z)$ with the measurement surface $\Gamma_{a,A}$ given by $A = 8$ and $a = 1.1, 2.0, 2.9$, respectively. Figures 6(d)–(f) present the imaging function $I(z)$ with the measurement surface $\Gamma_{a,A}$ given by with $a = 2$ and $A = 4, 7, 11$, respectively. It can be seen from figure 6 that the reconstructed result is getting

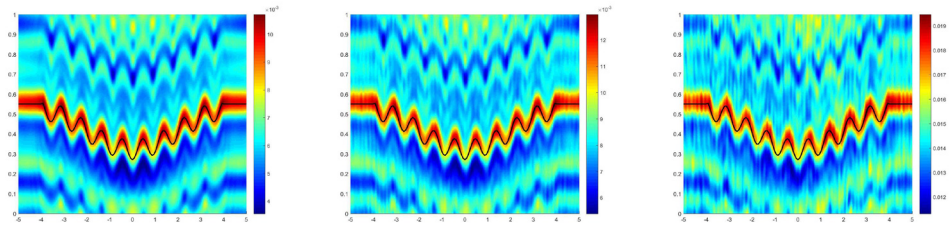

(a) (b) (c)

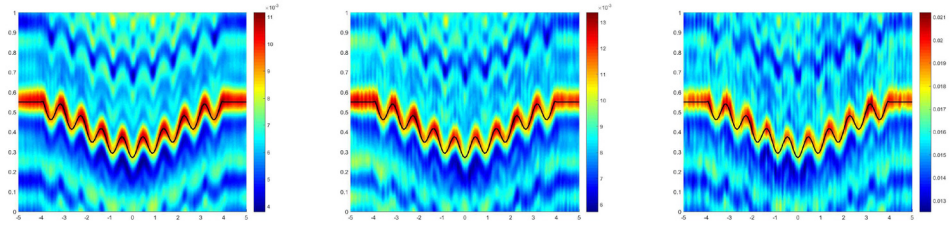

(d) (e) (f)

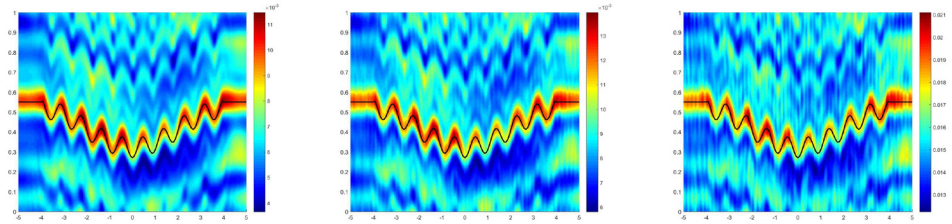

(g) (h) (i)

**Figure 4.** Reconstructed results from different kinds of measurement positions and from the data at different noise levels. (a) $\delta = 0$, straight line. (b) $\delta = 20\%$, straight line. (c) $\delta = 40\%$, straight line. (d) $\delta = 0$, random points. (e) $\delta = 20\%$, random points. (f) $\delta = 40\%$, random points. (g) $\delta = 0$, curve. (h) $\delta = 20\%$, curve. (i) $\delta = 40\%$, curve.

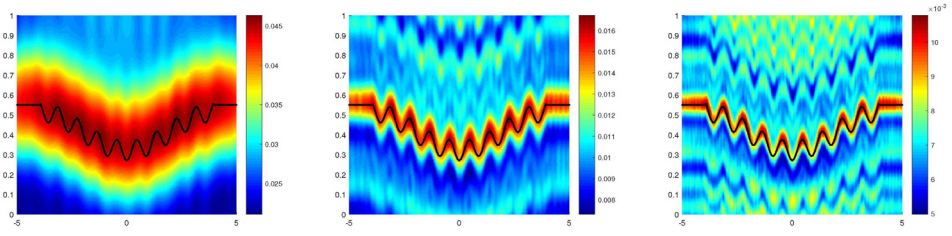

(a) (b) (c)

**Figure 5.** Reconstructed results of the imaging function $I(z)$ at different incident frequencies. (a) $\omega = 5$. (b) $\omega = 15$. (c) $\omega = 25$.

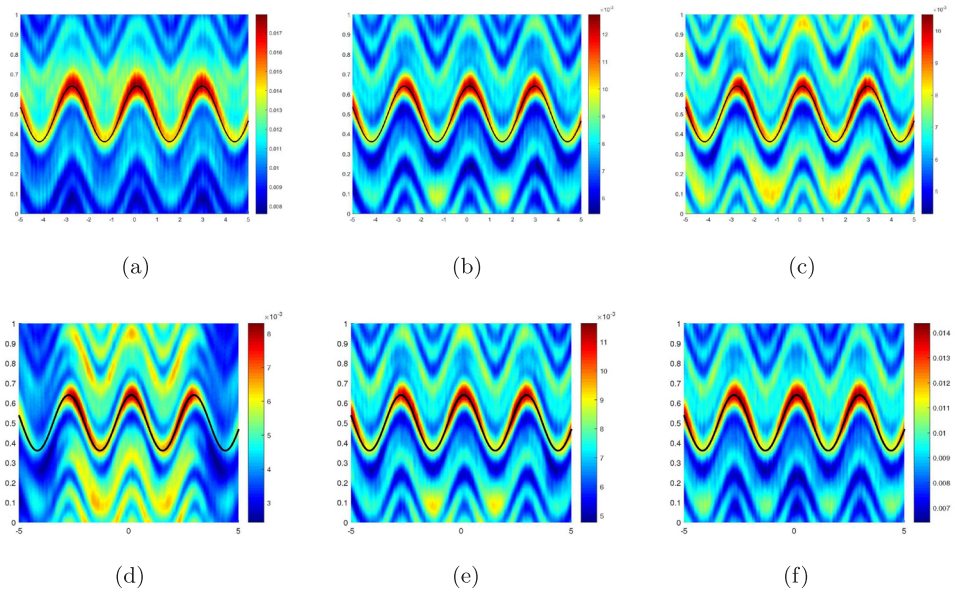

**Figure 6.** Reconstructed results of the imaging function $I(z)$ from the data at different line segments. (a) $\{(x_1, 1.1) \mid |x_1| < 8)\}$. (b) $\{(x_1, 2) \mid |x_1| < 8)\}$. (c) $\{(x_1, 2.9) \mid |x_1| < 8)\}$. (d) $\{(x_1, 2) \mid |x_1| < 4)\}$. (e) $\{(x_1, 2) \mid |x_1| < 7)\}$. (f) $\{(x_1, 2) \mid |x_1| < 11)\}$.

better if the measurement surface $\Gamma_{a,A}$ is getting closer to the rough surface or the length of $\Gamma_{a,A}$ is getting longer. However, a rigourous resolution analysis of our inversion algorithm with respect to the height and length of $\Gamma_{a,A}$ is still unclear to us.

**Example 4.** We investigate the performances of the imaging function $I(z)$ with different numbers of incident plane waves and measurement points (that is, $M$ and $N$). Since $M$ and $N$ represent respectively the discretization levels of the interval of incident angles and measurement positions, the choice of them do not depend on the numerical method we used in this paper. We consider the original rough surface $\Gamma$ with

$$f(x_1) = 0.5 + 0.16\sin(\pi x_1) + 0.1\sin(0.5\pi x_1).$$

Figures 7(a)–(c) present the reconstructed results of the imaging function $I(z)$ with $N = 401$ and $M = 64, 128, 256$, respectively. Figures 7(d)–(f) show the results of the imaging function $I(z)$ with $M = 256$ and $N = 51, 101, 201$, respectively. One can conclude from these experimental results that a larger number of incident plane waves and measurement points can help us improve the reconstructions. This is consistent with the fact that the function $I_A(z)$ in (3.12) could better approximates to the imaging function $I(z)$ if $M$ and $N$ are larger.

**Example 5.** We investigate the influence of different velocity contrasts for P and S waves on the reconstructed results. We consider the original rough surface $\Gamma$ with

$$f(x_1) = 0.5 + 0.084\sin(0.6\pi x_1) + 0.084\sin(0.48\pi x_1) + 0.03\sin(1.5\pi(x_1 - 1)).$$

The compressional wave velocity and shear wave velocity can be expressed as $c_p = \sqrt{\lambda + 2\mu}$ and $c_s = \sqrt{\mu}$, respectively. The velocity contrast $\tau$ is defined as $\tau = c_p/c_s$. Figure 8 present

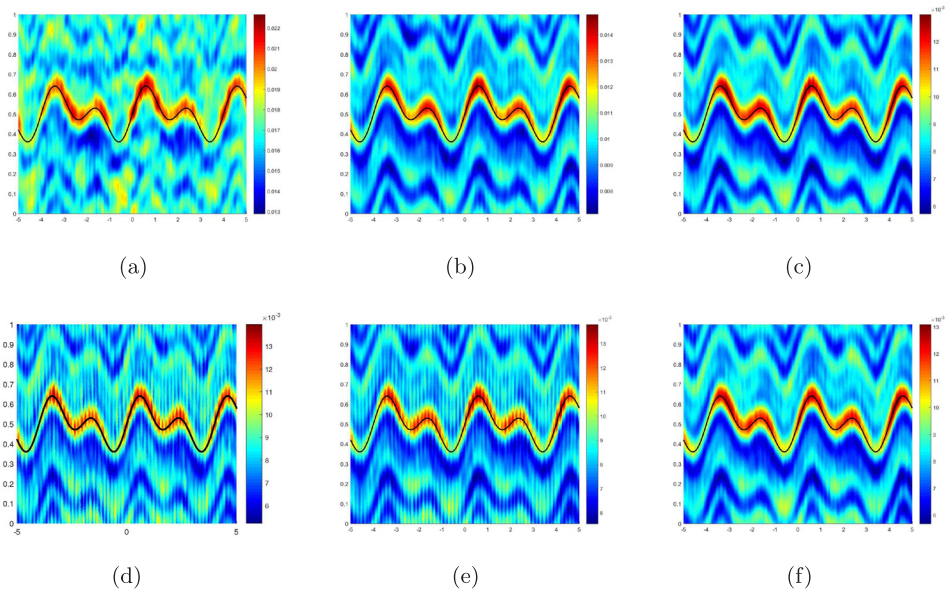

**Figure 7.** Reconstructed results of the imaging function $I(z)$ with different numbers of measurement points $N$ and incident plane waves $M$. (a) $M = 64, N = 401$. (b) $M = 128, N = 401$. (c) $M = 256, N = 401$. (d) $M = 256, N = 51$. (e) $M = 256, N = 101$. (f) $M = 256, N = 201$.

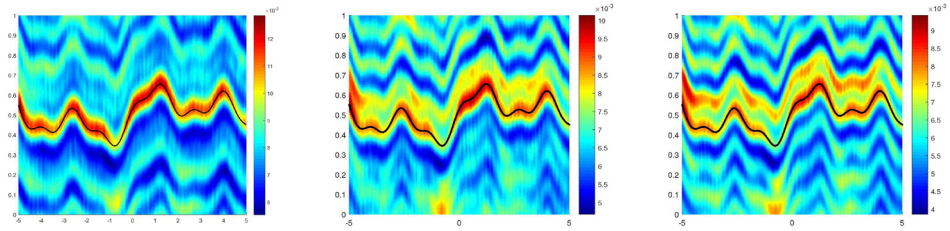

**Figure 8.** Reconstructed results of the imaging function $I(z)$ with different velocity contrasts $\tau$. (a) $\tau \approx 1.732$. (b) $\tau \approx 3.464$. (c) $\tau \approx 31.654$.

the reconstructed results of the imaging function $I(z)$ with the Lamé constant $\mu = 1$ and the Lamé constant $\lambda = 1, 10, 1000$, respectively, where the velocity contrast $\tau \approx 1.732, 3.464, 31.654$, respectively. From figure 8 we see that the reconstructed results deteriorate as the velocity contrast $\tau$ become larger. However, our method still works for the case with large contrast $\tau \approx 31.654$.

**Example 6.** We study the influence of different polarization directions $\boldsymbol{e}_j$ $(j = 1, 2)$ appeared in (3.6) and different kinds of incident waves on the reconstructed results. The original rough surface $\Gamma$ is given by

$$f(x_1) = 0.5 + 0.1\exp[-(0.75x_1 - 2.5)^2] + 0.2\exp[-(1.05x_1 - 4.2)^2] - 0.25\exp[-0.6x_1^2].$$

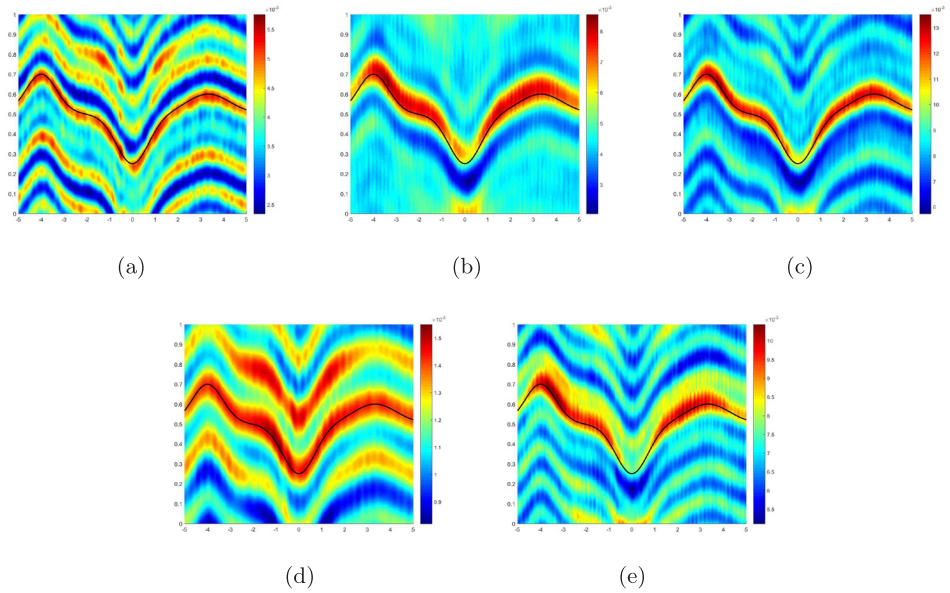


**Figure 9.** Imaging results with different polarizations and different types of incident plane waves. (a) Using only $p_1 = \boldsymbol{e}_1$. (b) Using only $p_2 = \boldsymbol{e}_2$. (c) $I$. (d) $I_{\mathrm{p}}^{\mathrm{in}}$. (e) $I_{\mathrm{s}}^{\mathrm{in}}$.

First, we consider the case of different polarization directions. Figures 9(a)–(c) show the results using (a) only the polarization $p_1 = \boldsymbol{e}_1$; (b) only the polarization $p_2 = \boldsymbol{e}_2$; (c) the indicator function (3.12). Secondly, we consider the case of different kinds of incident waves. Figures 9(d) and (e) are the reconstructed results with only incident compressional plane wave $\boldsymbol{u}_{\mathrm{p}}^{\mathrm{in}}(x;\boldsymbol{d}) := \boldsymbol{d}\mathrm{e}^{\mathrm{i}k_{\mathrm{p}}\boldsymbol{d}\cdot x}$ and incident shear plane wave $\boldsymbol{u}_{\mathrm{s}}^{\mathrm{in}}(x;\boldsymbol{d}) := \boldsymbol{d}^{\perp}\mathrm{e}^{\mathrm{i}k_{\mathrm{s}}\boldsymbol{d}\cdot x}$, respectively, where the corresponding indicator functions are given by

$$I_{\mathrm{p}}^{\mathrm{in}}(z) := \sum_{j=1}^{2} \int_{\Gamma_a} \left| \boldsymbol{U}_{\mathrm{p}}^{\mathrm{sc}}(x;z,\mathbf{e}_j) \right|^2 \mathrm{d}s(x),$$

$$I_{\mathrm{s}}^{\mathrm{in}}(z) := \sum_{j=1}^{2} \int_{\Gamma_a} \left| \boldsymbol{U}_{\mathrm{s}}^{\mathrm{sc}}(x;z,\mathbf{e}_j) \right|^2 \mathrm{d}s(x),$$

respectively, where $\boldsymbol{U}_{\mathrm{p}}^{\mathrm{sc}}(x;z,\mathbf{e}_j)$ and $\boldsymbol{U}_{\mathrm{s}}^{\mathrm{sc}}(x;z,\mathbf{e}_j)$ are defined in remark 3.4. We conclude that the polarization $p_1$ can capture the rough surface accurately but with some sidelobes, while the polarization $p_2$ can only find the convex part of the surface but with few sidelobes. If we combine them together, that is, using our imaging function (3.11), the result can be improved since it inherits the advantages of the two polarizations. Further, using only the compressional or the shear wave to be the incident wave can also find the profile of the rough surface. However, the reconstructions are not as good as before since the combination of these two waves can inherit the merits of both waves.

**Example 7.** In order to fully exploit the nature of elastic scattering problems, we consider partial measurements of (i) only compressional part or shear part of the corresponding scattered waves, and (ii) only the $e_1$-component or $e_2$-component of the corresponding scattered waves. The rough surface in this example is given as follows

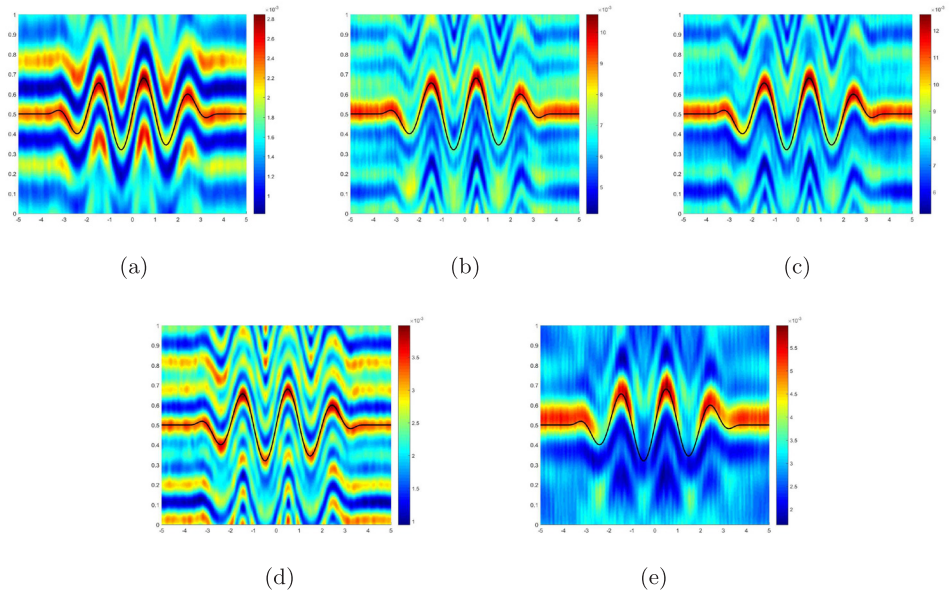


**Figure 10.** Imaging results with partial measurements. (a) $I_{\mathrm{p}}^{\mathrm{sc}}$. (b) $I_{\mathrm{s}}^{\mathrm{sc}}$. (c) $I$. (d) Only $e_1$-component of the scattered wave. (e) Only $e_2$-component of the scattered wave.

$$f_6(x_1) = \begin{cases} 0.5 + 0.5\exp[16/(x_1^2 - 16)]\sin(\pi x_1) & x_1 < 4, \\ 0.5 & \text{else.} \end{cases}$$

We first consider case (i). For $\alpha = p, s$, denote the compressional part and the shear part of the scattered data $u_\alpha^{\mathrm{sc}}$ by $\boldsymbol{u}_\alpha^{sc,\boldsymbol{P}}$ and $\boldsymbol{u}_\alpha^{sc,\boldsymbol{S}}$, respectively. Accordingly, the imaging functions for the compressional and shear waves are given by

$$I_{\mathrm{p}}^{\mathrm{sc}}(z) := \frac{1}{64\pi^2}\sum_{j=1}^{2}\int_{\Gamma_a}\left|\frac{1}{\lambda+2\mu}\left[\int_{\mathbb{S}_-}\boldsymbol{u}_{\mathrm{p}}^{sc,\boldsymbol{P}}(x;\boldsymbol{d})d_j\mathrm{e}^{-\mathrm{i}k_p z\cdot\boldsymbol{d}}\mathrm{d}s(\boldsymbol{d}) - \int_{\mathbb{S}_-} d_j'\boldsymbol{d}'\mathrm{e}^{\mathrm{i}k_{\mathrm{p}}(x'-z')\cdot\boldsymbol{d}}\mathrm{d}s(\boldsymbol{d})\right]\right.$$
$$\left. + \frac{1}{\mu}\int_{\mathbb{S}_-}\boldsymbol{u}_{\mathrm{s}}^{sc,\boldsymbol{P}}(x;\boldsymbol{d})d_j^{\perp}\mathrm{e}^{-\mathrm{i}k_{\mathrm{s}}\mathbf{z}\cdot\boldsymbol{d}}\mathrm{d}s(\boldsymbol{d})\right|^2\mathrm{d}s(x),$$

$$I_{\mathrm{s}}^{\mathrm{sc}}(z) := \frac{1}{64\pi^2}\sum_{j=1}^{2}\int_{\Gamma_a}\left|\frac{1}{\mu}\left[\int_{\mathbb{S}_-}\boldsymbol{u}_{\mathrm{s}}^{sc,\boldsymbol{S}}(x;\boldsymbol{d})d_j^{\perp}\mathrm{e}^{-\mathrm{i}k_{\mathrm{s}}\mathbf{z}\cdot\boldsymbol{d}}\mathrm{d}s(\boldsymbol{d}) - \int_{\mathbb{S}_-}(d')_j^{\perp}(\boldsymbol{d}')^{\perp}\mathrm{e}^{\mathrm{i}k_{\mathrm{s}}(x'-z')\cdot\boldsymbol{d}}\mathrm{d}s(\boldsymbol{d})\right]\right.$$
$$\left. + \frac{1}{\lambda+2\mu}\int_{\mathbb{S}_-}\boldsymbol{u}_{\mathrm{p}}^{sc,\boldsymbol{S}}(x;\boldsymbol{d})d_j\mathrm{e}^{-\mathrm{i}k_p z\cdot\boldsymbol{d}}\mathrm{d}s(\boldsymbol{d})\right|^2\mathrm{d}s(x),$$

respectively. Figures 10(a)–(c) present the reconstructed results of the imaging function $I_{\mathrm{p}}^{\mathrm{sc}}$, $I_{\mathrm{s}}^{\mathrm{sc}}$ and $I$, respectively. Secondly, we consider case (ii). In this case, we only measure the $e_1$-component or the $e_2$-component of the scattered wave. Accordingly, we use the imaging function (3.11) with the vector field $\boldsymbol{U}^{\mathrm{sc}}$ replaced by its $e_1$ or $e_2$-component. The reconstructed results (see figures 10(d)–(e)) are not as good as that using both $e_1$ and $e_2$-components shown in figure 10(c). This phenomenon makes a sense physically, but it remains unclear to us how to interpret the difference between figures 10 (d) and (e). From figure 10, it can be seen that dif-

ferent types of measurement data could lead to different imaging results. This may be caused by the coupling property of compressional and shear waves in linear elasticity.

The above numerical examples illustrate that our imaging method gives a good and stable reconstruction of the unbounded rigid rough surface. In particular, the imaging algorithm is very robust to noisy data. Further, the numerical results in figures 8–10 show that our imaging method exploits specificities of elastic scattering problems, which did not occur in the case of the Helmholtz equation [30].

## 5. Conclusion

We proposed a non-iterative imaging method for recovering unbounded rigid rough surfaces from near-field data in linear elasticity. Thanks to the Funk–Hecke formula and the free-field Green's tensor for the Navier equation, an imaging function is proposed to reconstruct an unbounded rigid rough surface. The imaging function can be easily implemented since only the calculation of inner products is involved. Numerical experiments have been carried out to demonstrate the effectiveness of our method and to show the influence of reconstructed results on different parameters. It can be concluded that the inverse elastic scattering problems are much different from the case of the scalar Helmholtz equation, due to different types of incoming waves, multiple choice of polarization directions and a variety of partial measurements. Moreover, the influence of polarization directions and components of the scattered wave on the reconstructed results need to be investigated theoretically. A more thoroughly theoretical resolution analysis due to different parameters needs to be done in the near future to enhance the comprehension of our proposed method and even to improve the proposed imaging functional. Further, the imaging algorithm could be extended to many other cases such as inverse electromagnetic scattering problems by unbounded rough surfaces and the inverse elastic problems in 3D. Progress in these directions will be reported in the near future.

## Acknowledgments

We thank the handling editor and the referees for their careful reviews, constructive comments and suggestions which helped to improve the presentation of the paper. This work is partly supported by the NSFC of China grants 91630309, 11501558, 11571355, 11671028 and 11871466, and the NSAF grant U1530401.

## ORCID iDs

Guanghui Hu https://orcid.org/0000-0002-8485-9896
Bo Zhang https://orcid.org/0000-0001-7355-0941
Haiwen Zhang https://orcid.org/0000-0003-4035-4754

## References

[1] Ammari H, Garnier J, Jugnon V and Kang H 2012 Direct reconstruction methods in ultrasound imaging of small anomalies *Mathematical Modeling in Biomedical Imaging* II (*Lecture Notes in Mathematics* vol 2035) (Heidelberg: Springer) pp 31–55

[2] Ammari H, Garnier J, Jugnon V and Kang H 2012 Stability and resolution analysis for a topological derivative based imaging functional *SIAM J. Control Optim.* **50** 48–76

[3] Andrews G E, Askey R and Roy R 1999 *Special Functions* (Cambridge: Cambridge University Press) (https://doi.org/10.1017/CBO9781107325937)
[4] Arens T 2000 The scattering of elastic waves by rough surfaces *PhD Thesis* Brunel University, UK
[5] Arens T 2001 Uniqueness for elastic wave scattering by rough surfaces *SIAM J. Math. Anal.* **33** 461–76
[6] Arens T 2002 Existence of solution in elastic wave scattering by unbounded rough surfaces *Math. Methods Appl. Sci.* **25** 507–28
[7] Bellis C, Bonnet M and Cakoni F 2013 Acoustic inverse scattering using topological derivative of far field measurements-based $L^2$ cost functionals *Inverse Problems* **29** 075012
[8] Bonnet M and Constantinescu A 2005 Inverse problems in elasticity *Inverse Problems* **21** 1–50
[9] Guzina B B and Bonnet M 2004 Topological derivative for the inverse scattering of elastic waves *Quart. J. Mech. Appl. Math.* **57** 161–79
[10] Chikichev I and Guzina B B 2008 Generalized topological derivative for the Navier equation and inverse scattering in the time domain *Comput. Methods Appl. Mech. Eng.* **197** 4467–4484
[11] Chen J, Chen Z and Huang G 2013 Reverse time migration for extended obstacles: acoustic waves *Inverse Problems* **29** 085005
[12] Chen Z and Huang G 2015 Reverse time migration for extended obstacles: elastic waves (in Chinese) *Sci. Sin. Math.* **45** 1103–14
[13] Colton D and Kress R 2013 *Inverse Acoustic and Electromagnetic Scattering Theory* 3rd edn (New York: Springer)
[14] Colton D and Kirsch A 1996 A simple method for solving inverse scattering problems in the resonance region *Inverse Problems* **12** 383–93
[15] Ding M, Li J, Liu K and Yang J 2017 Imaging of local rough surfaces by the linear sampling method with near-field data *SIAM J. Imaging Sci.* **10** 1579–602
[16] Elschner J and Hu G 2012 Elastic scattering by unbounded rough surfaces *SIAM J. Math. Anal.* **44** 4101–27
[17] Elschner J and Hu G 2012 An optimization method in inverse elastic scattering for one-dimensional grating profiles *Commun. Comput. Phys.* **12** 1434–60
[18] Elschner J and Hu G 2015 Elastic scattering by unbounded rough surfaces: solvability in weighted Sobolev spaces *Appl. Anal.* **94** 251–78
[19] Feijoo G R 2004 A new method in inverse scattering based on the topological derivative *Inverse Problems* **20** 1819–40
[20] Guzina B B and Pourahmadian F 2015 Why the high-frequency inverse scattering by topological sensitivity may work *Proc. R. Soc.* A **471** 20150187
[21] Hu G, Lu Y and Zhang B 2013 The factorization method for inverse elastic scattering from periodic structures *Inverse Problems* **29** 115005
[22] Ito K, Jin B and Zou J 2012 A direct sampling method to an inverse medium scattering problem *Inverse Problems* **28** 025003
[23] Ji X, Liu X and Xi Y 2018 Direct sampling methods for inverse elastic scattering problems *Inverse Problems* **34** 035008
[24] Landau L and Lifshitz E 1986 *Theory of Elasticity* (Oxford: Pergamon)
[25] Li J, Sun G and Zhang R 2016 The numerical solution of scattering by infinite rough interfaces based on the integral equation method *Comput. Math. Appl.* **71** 1491–502
[26] Li J, Liu X, Zhang B and Zhang H 2018 A Nyström method for elastic scattering by unbounded rough surfaces based on the integral equation technique in preparation
[27] Li P, Wang Y and Zhao Y 2015 Inverse elastic surface scattering with near-field data *Inverse Problems* **31** 035009
[28] Li P, Wang Y, Wang Z and Zhao Y 2016 Near-field imaging of biperiodic surfaces for elastic waves *J. Comput. Phys.* **324** 1–23
[29] Liu X 2017 A novel sampling method for multiple multiscale targets from scattering amplitudes at a fixed frequency *Inverse Problems* **33** 085011
[30] Liu X, Zhang B and Zhang H 2018 A direct imaging method for inverse scattering by unbounded rough surfaces *SIAM J. Imaging Sci.* **11** 1629–50
[31] Potthast R 2010 A study on orthogonality sampling *Inverse Problems* **26** 074015
[32] Santosa F 1984 *Inverse Problems of Acoustic and Elastic Waves* F Santosa ed (Philadelphia, PA: SIAM)